Editors' Suggestion

Transient electron scavengers modulate carrier density at a polar/nonpolar perovskite oxide heterojunction

Widitha S. Samarakoon,[1,2] Peter V. Sushko,[2,*] Dooyong Lee,[3] Bharat Jalan,[3] Hua Zhou,[4] Yingge Du,[2] Zhenxing Feng,[1,†] and Scott A. Chambers[2]

[1]*School of Chemical, Biological and Environmental Engineering, Oregon State University, Corvallis, Oregon 97331, USA*
[2]*Physical and Computational Sciences Directorate, Pacific Northwest National Laboratory, Richland, Washington 99354, USA*
[3]*Department of Chemical Engineering and Materials Science, University of Minnesota, Minneapolis, Minnesota 55455, USA*
[4]*Advanced Photon Source, Argonne National Laboratory, Lemont, Illinois 60439, USA*

(Received 28 February 2022; accepted 27 September 2022; published 19 October 2022)

We show how transient electron scavengers can be utilized to control the carrier concentration at polar/nonpolar perovskite interfaces. By combining quantitative synchrotron x-ray-based interface structure determination with *ab initio* modeling, we demonstrate that Nd vacancy formation and the resulting formation of Nd adatoms, stabilized by oxygen scavengers at the growth front, can quantitatively account for the decreased carrier concentration at the $SrTiO_3/n$ $NdTiO_3/SrTiO_3(001)$ heterojunction for $n = 1$ unit cell. This study yields insight into growth mechanisms and the effect of transient species and defects on the electronic properties of oxide heterojunctions.

DOI: 10.1103/PhysRevMaterials.6.103405

I. INTRODUCTION

Oxide heterostructures that facilitate the formation of high-carrier-density two-dimensional (2D) electron gases (2DEGs) are promising candidates for novel classes of devices in oxide electronics. The design of oxide heterostructures with low-dimensional conductive channels has led to the emergence of new functional properties [1–3]. Unlike conventional semiconductor heterostructures, complex oxide heterostructures can exhibit strong correlation effects [4–6], high 2D electron densities ($\sim 10^{14}$ cm^{-2}), and high breakdown voltages. Devices, such as plasmonic field-effect transistors, rely on the plasma wave velocity which is directly proportional to the 2DEG density [7]. Predictive control of 2DEG densities in oxide heterostructures could transform the field of nanoscale electronic devices.

One such archetype system is the $NdTiO_3/SrTiO_3(001)$ heterojunction (NTO/STO). 2DEG formation in NTO/STO grown using hybrid molecular beam epitaxy (h-MBE), occurs at the internal polar/nonpolar interfaces in layered structures consisting of both single interfaces and superlattices [3]. In the absence of electrically active defects, a 2DEG can emerge from the presence of a polar discontinuity at a polar/nonpolar interface [8]. The 2D conductivity stems from electronic reconstruction (ER) that alleviates the polar discontinuity resulting from the formation of atomically abrupt interfaces (see Supplemental Material, Fig. S1 [9]). It was demonstrated [3] (Fig. S1 [9]) that STO/NTO (2 u.c.)/STO grown on (001)-oriented $(LaAlO_3)_{0.3}(Sr_2TaAlO_6)_{0.7}$ LSAT (NTO × 2) using h-MBE exhibits metallic conductivity with a carrier density (n_{2D}) equal to $\sim 1\ e^-$ per lateral u.c. of NTO ($0.5\ e^-$ per NTO/STO interface), which quantitatively matches the expected value in the ER model [10]. In contrast, STO/NTO (1 u.c.)/STO on LSAT (001) (NTO × 1) exhibits n_{2D} of only $0.5\ e^-$ per u.c. of NTO, which is half the value expected from the ER model. While n_{2D} in NTO × n ($n \geqslant 2$) on LSAT (001) can be reduced via the controlled introduction of Nd vacancies (V_{Nd}), which results in hole doping [3], the lower-than-expected n_{2D} in NTO × 1 was observed under growth conditions that do not create V_{Nd} in NTO × n ($n \geqslant 2$).

To establish the origin of the markedly lower n_{2D} in NTO × 1, we examine the relationship between the atomic structure and composition of NTO × 1 and NTO × 2, and atomic-scale processes at the STO/NTO growth front. Specifically, we examine how interaction of oxygen species with Ti^{3+} species at the growth front induces the electron charge redistribution and a corresponding ionic rearrangement that, in turn, results in the formation of vacancies, cation intermixing at the STO/NTO interfaces, and depletion of the electron density in the conduction band.

It is well established that controlled annealing in an oxygen-rich environment can fill oxygen vacancies [11,12] and promote cation ordering [13]. In the presence of molecular oxygen, the concentration of persistently trapped electron and hole centers can be increased by a factor of 10 due to the ability of O_2 to scavenge photoexcited electrons and form adsorbed O_2^- species [14]. Furthermore, annealing oxides in oxygen or air can produce cation vacancies [15] and cause phase transformations altogether [16,17]. Yet, elementary atomic-scale mechanisms that underpin these phenomena are challenging to deconvolute.

By combining surface x-ray diffraction (SXRD) and coherent Bragg rod analysis (COBRA) [18–22] of a well-defined model system with *ab initio* modeling, we developed a

*peter.sushko@pnnl.gov
†zhenxing.feng@oregonstate.edu

physical model that explains the dramatic decrease of n_{2D} in going from NTO × 2 to NTO × 1 and provides insight into the origin of the V_{Nd} and the effect of transient surface species on vacancy formation. We also confirmed that V_{Nd} becomes detectable only in the limit of a single NdO atomic plane, for which the fractional V_{Nd} concentration reaches ∼1/6–1/8. This study illustrates how mechanistic understanding of defect-induced behavior in oxide heterostructures is facilitated by examining material properties in the limit of single u.c. thick layers and provides insight into the materials transformation induced by interaction with oxygen species.

II. EXPERIMENT AND MODELING

The NTO × 1 and NTO × 2 heterostructures were grown on (001)-oriented $(LaAlO_3)_{0.3}(Sr_2TaAlO_6)_{0.7}$ (LSAT) substrates (Crystech GmbH, Germany) using h-MBE (traditionally known as metal-organic or organometallic MBE). The STO thickness was held constant at 8 u.c. for both the buffer layer and the capping layer unless specified otherwise. A ∼500-nm-thick Ta layer was sputter deposited at room temperature on the back of the substrate prior to film growth to improve heat transfer between the film and the substrate heater. Titanium tetra-isopropoxide (TTIP) (99.999% from Sigma-Aldrich, USA) was utilized as the metal-organic precursor for the Ti source, and solid elemental sources for Nd (99.99% from Ames Lab, USA) and Sr (99.99% from Sigma-Aldrich, USA). No additional oxygen was used since TTIP supplies ample oxygen. The substrate temperature was held at 900 °C. The use of TTIP in metal-organic MBE does not leave behind any measurable carbon or other unintentional impurities in perovskite films. *In situ* reflection high-energy electron diffraction was used to monitor film growth in real time. Details of the growth, stoichiometry control, and structural characterization of these films using *ex situ* high-resolution x-ray diffraction (XRD), atomic force microscopy (AFM), and x-ray photoelectron spectroscopy (XPS) were discussed elsewhere [23].

The layer-resolved atomic structure and Nd concentrations in the NTO layers were quantitatively determined using SXRD measurements at beamline 33-ID of the Advanced Photon Source at Argonne National Laboratory. SXRD diffraction intensities along the substrate-defined Bragg rods were measured using methodologies described previously [24]. Since the measured diffracted intensities reveal only the amplitude of the complex structure factors, the COBRA method was used to iteratively retrieve phase information and subsequently fully reconstruct the model-independent, 3D electron density (ED) maps of the films as described below.

The STO/NTO/STO superlattice was represented using the periodic slab model. The STO layer at the substrate was 3 u.c. thick and the NTO layer containing either 1 or 2 u.c. was capped with 1-u.c.-thick STO film. To investigate the effect of defect concentration, including V_{Nd} and surface adsorbents, we considered several lateral cells with areas ranging from $a_0 \times a_0$ (1 × 1 for short) to $2\sqrt{2} \times 2\sqrt{2}$, where a_0(3.868 Å) is the in-plane lattice parameter of the LSAT substrate. The calculations were performed using the VASP package [25] and the PBEsol density functional [26]. Since the accuracy of generalized gradient approximation exchange-correlation

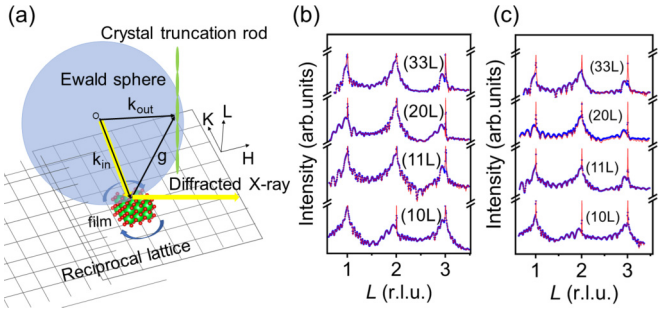

FIG. 1. (a) The experimental geometry for synchrotron x-ray diffraction measurements used in COBRA. (H, K, L) are coordinate axes in the reciprocal space defined by the orientation of the substrate. k_{in} and k_{out} are the incident and the outgoing x-ray wave vectors and g is the momentum transfer vector. Measured crystal truncation rods (CTRs) for (b) NTO × 1 and (c) NTO × 2. The experimental diffraction intensities versus the reciprocal lattice unit (r.l.u.) are shown using blue dots; the corresponding COBRA fits are shown with solid red lines.

functionals is affected by self-interaction error, the Hubbard U correction (within the PBEsol + U scheme) for the Ti 3d states was applied in selected calculations [27]. The value of U (2.8 eV) was optimized to reproduce the one-electron bandgap of bulk NTO [3,10]. All calculations were performed in the spin-polarized mode. The projector-augmented wave potentials were used to approximate the effect of the core electrons [28]. The Γ-centered k mesh was varied from 8 × 8 × 1 to 2 × 2 × 1 depending on the size of the lateral cell. The plane-wave basis-set cutoff was set to 400 eV. The total energy convergence criterion was set to 10^{-5} eV. Bader charge population analysis was used [29]. One-electron densities of states (DOS) were smeared out by convoluting band energies with Gaussian functions with the full width at half maximum of 0.2 eV. Nd diffusion activation energies were calculated using the climbing-image nudged elastic band (CI-NEB) method and eight NEB images [30] and the Γ point only for the $2\sqrt{2} \times 2\sqrt{2}$ lateral cell. The binding energies of oxygen species were calculated with respect to the triplet state of the gas-phase O_2 molecule.

III. RESULTS AND DISCUSSION

The 3D ED profiles for the NTO × 1 and NTO × 2 heterostructures were reconstructed using COBRA. The diffraction measurements were conducted at an incident photon energy of 20 keV and the x-ray beam size was 0.1 mm by 0.3 mm in horizontal and vertical directions with respect to the sample stage, respectively [Fig. 1(a)]. Ten symmetry-inequivalent Bragg rods were recorded up to $L_{max} = 4.5$ r.l.u. (reciprocal lattice units) using a pixel array area detector (Dectris PILATUS 100 K model). For the specular (00L) rod, the incident angle and the exit angles were kept the same, whereas the incident angle was maintained at 5° for off-specular rods (10L), (11L), (20L), (21L), (22L), (30L), (31L), (32L), and (33L). The raw data were subjected to background subtraction and corrected for any malfunctioning and irregularity in the photoresponse of pixels in the detector using a flat-field file. Then, the resulting intensities were integrated in two

dimensions, normalized, and corrected to account for the Lorentz factor, beam polarization, and active area of the beam on the film surface [24,31,32].

The initial crystallographic COBRA model consisted of a bulk LSAT substrate and coherently strained (in both in-plane directions) STO and NTO films with atomic positions in the out-of-plane direction defined by their respective bulk lattices (Table S1 [9]). By scaling the Debye Waller (DW) factors used in the fitting, we allowed for larger deformation of the atomic layers near the surface (DW ~ 0.25) than in the bulk (DW ~ 0.1). The fitting was performed using an iterative difference algorithm; the calculated diffraction intensities were compared to the experimental diffraction intensities by summing over contributions for each rod (k) using the overall x-ray reliability factor, defined as

$$R = \frac{\sum_k ||F(k)_m| - |F(k)_c||}{\sum_k |F(k)_m|} \quad (k = 1, \ldots, 10),$$

where $|F_m|$ and $|F_c|$ are the measured (m) and calculated (c) diffraction amplitudes, respectively. Finally, the optimized 3D ED was integrated over the substrate-defined unit cell volume in three dimensions and normalized to the substrate reference atom (e.g., La/Sr assumed to retain their nominal electron number) to obtain the electron number for each atomic position as a function of film thickness [24,31,32].

Comparison of the experimental and calculated diffraction intensities along (10L), (11L), (20L), and (33L) Bragg rods reveals a good match for both NTO × 1 and NTO × 2 heterostructures [Figs. 1(b) and 1(c)] with the R factors of 3.5% and 4.1%, respectively. Figures 2(a)–2(c) show ED profiles for NTO × 1 along three high symmetry atomic columns parallel to the out-of-plane direction. Figures 2(d)–2(f) show the corresponding ED profiles for NTO × 2. The peaks in ED profiles, representing the positions of corresponding atoms, are clearly resolved indicating that both structures are highly ordered and coherently strained to the LSAT substrate. The integral of these ED peaks is proportional to the average electron number (EN) of the corresponding atoms (e.g., 43.7 for La/Sr in LSAT) and can be used to quantify the occupation of atoms. The sharp ED changes along the (0 0 z) line and the increase in ED along the (0.5 0.5 z) line at the LSAT/STO interface are attributed to the changes in the average EN of the A sites and B sites, respectively. Since STO and NTO have the same B-site cation (Ti), the peaks in the ED line profiles remain nearly constant across the STO/NTO/STO junction throughout the film except at the surface [Figs. 2(b) and 2(e)]. The reduction in the A- and B-site ED magnitude near the film surface is attributed to incomplete atomic layer coverage and roughness effects at the film surface, which have been observed in MBE and PLD grown films [33,34].

We note that due to the limited sampling range in reciprocal space (up to the maximum L value in CTR measurement), small-scale electron density fluctuations below and above zero value can be expected from the Fourier phase retrieval iterative process. The small negative electron density values shown in Fig. 2 represent a common experimental artifact in the Fourier phase retrieval algorithm that generates the obtained electron density profile with respect to the measured crystal truncation rod diffraction data. The actual electron density is

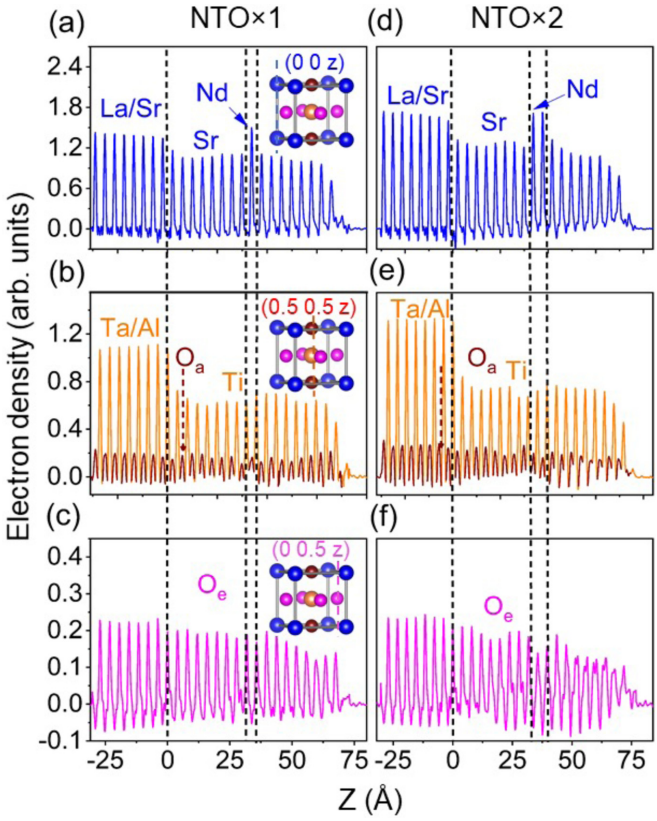

FIG. 2. COBRA-determined electron density profiles for NTO × 1 (left) and NTO × 2 (right) along the (a), (d) (0 0 z) line passing through La/Sr atoms in LSAT, Sr atoms in STO, and Nd atoms in NTO, (b), (e) (0.5 0.5 z) line passing through Ta/Al atoms in LSAT, Ti atoms in STO and NTO, and apical oxygen atoms (O_a), (c), (f) (0 0.5 z) line passing through equatorial oxygen atoms (O_e). Insets show the corresponding crystal models. Black dashed lines indicate the STO/LSAT interface, the NTO/STO interface, and the STO capping layer interface with NTO.

superimposed on top of such small fluctuations. These fluctuations are more pronounced for lighter elements, such as oxygen atomic line. It is a standard approach to put the base line (visible at $Z > 75$ Å in each panel in Fig. 2) at zero after the phase retrieval reconstruction is completed. This approach is described in detail elsewhere [35].

The uncertainty of the site occupancies can be as large as ±15% for O, but as low as ±5% for heavier atoms at the A and B sites [31,33,34]. A slight increase in the EN near the STO/LSAT interface (Fig. 3), especially for the B site, is attributed to the mixed termination $[(Al_{1-x}Ta_xO_2)_{1-\delta}(Sr_{1-y}La_yO)_\delta]$ commonly observed in LSAT(001) [19]. An abrupt increase in EN for the A-site cation at the bottom NTO/STO interface indicates that this interface is atomically sharp.

In contrast, EN in the first formally SrO layer on the NTO film is larger than that in pure STO, which points to Nd-Sr intermixing; this effect is more pronounced in NTO × 2 than in NTO × 1 (Fig. 3). This observation provides an independent confirmation of reported atomically sharp NTO/STO interfaces and relatively diffuse STO/NTO interfaces in a $\{[NTO]_{16}/[STO]_8\}_3$ superlattice on LSAT [10].

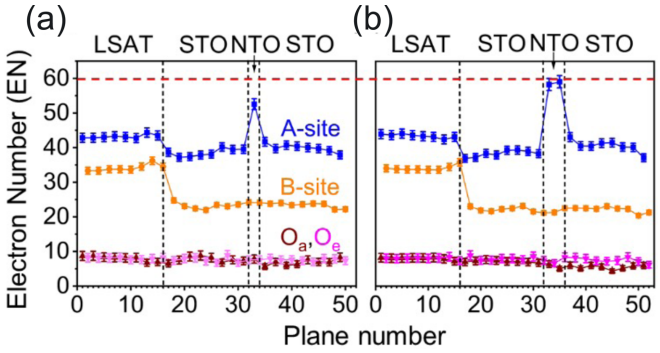

FIG. 3. Electron numbers (EN) for each atomic site depending on the plane number for (a) NTO × 1 and (b) NTO × 2. O_a and O_e represent apical and equatorial oxygens, respectively. The positions of the STO/LSAT, the lower NTO/STO, and the upper STO/NTO interfaces are shown with dashed black lines. The red dashed line shows the nominal EN of 60 for Nd. The error bars for the EN are calculated using the COBRA error analysis [33,34].

The EN values also reveal the presence of inhomogeneities, such as vacancies. For example, the EN for the Nd site in NTO × 1 is lower than the nominal value of 60 [Fig. 3(a)]. In contrast, the EN for the Nd sites in NTO × 2 [Fig. 3(b)] agree well with the nominal value, within the uncertainty of this analysis. Since NTO × 1 shows negligible intermixing at the STO/NTO interface, we attribute the lower EN values to the presence of V_{Nd}. For comparison, V_{Nd} are not detectable in NTO × 2. The presence of V_{Nd} in NTO × 1 is consistent with the lower-than-expected n_{2D} observed, as discussed previously in the context of the ER model for intentionally V_{Nd}-doped $Nd_{1-x}TiO_3$ layers encapsulated in STO [3].

To find the V_{Nd} concentration (denoted as $[V_{Nd}]$) in NTO × 1 expected from the ER model, we equate the observed n_{2D} per interface (0.25 e^-) to the number of electrons donated by the $Nd_{1-x}O$ layer to each neighboring TiO_2 plane (Fig. S1 [9]), $1/2(1–3[V_{Nd}])$ e^-. The resulting $[V_{Nd}]$ (0.167) can be compared with $[V_{Nd}]$ from COBRA. According to COBRA error analysis [33,34], the Nd EN values for NTO × 1 vary from 51.0 to 54.1. Then, $[V_{Nd}] = \frac{60-EN}{60}$ is between 0.10 and 0.15, in reasonable agreement with the $[V_{Nd}]$ value determined using transport measurements [3].

To reveal the origin of V_{Nd} in NTO × 1, we first examine the dependence of the vacancy formation energy (E_{V-Nd}) on the $[V_{Nd}]$ using *ab initio* simulations (Fig. S2 [9]). In the limit of maximum $[V_{Nd}]$ (one V_{Nd} per 1 × 1 lateral cell), the Ti 3*d*-derived NTO conduction band (CB) is emptied *and* two holes (h^+) form in the O 2*p* valence band (VB). E_{V-Nd} drops steeply with decreasing $[V_{Nd}]$ until the number of h^+ in the VB is zero. Since the formation of h^+ in the VB is energetically costly and known to result in material degradation via emission of O atoms [36], we can put an upper bound on $[V_{Nd}]$ of 1/3 per 1 × 1 lateral cell. As $[V_{Nd}]$ is decreased further, its effect on E_{V-Nd} becomes less pronounced. A similar trend in E_{V-Nd} vs $[V_{Nd}]$ is observed for NTO × 2. Notably, the calculated E_{V-Nd} per the same unit area is smaller in NTO × 2 than in NTO × 1, suggesting that if V_{Nd} formation is driven by thermodynamics alone, $[V_{Nd}]$ would be larger in NTO × 2 than in NTO × 1. Since our experimental data point to the existence of V_{Nd} in NTO × 1 but not in NTO × 2, we propose that this simple thermodynamic model is inadequate and, instead, examine in detail atomic scale kinetic processes at the NTO/STO growth front.

We note that in h-MBE synthesis of STO/NTO/STO, Ti and O atoms are supplied in the form of a metal-organic precursor (titanium tetra-isopropoxide [3,10]) and that the amount of O supplied exceeds the stoichiometric requirement. Excess oxygen may accumulate at the sample surface during NTO growth in either atomic (O) or molecular (O_2) form and participate in surface chemical reactions. Our calculations show that TiO_2-terminated NTO/STO can bind excess oxygen at surface Ti sites and that adsorbed O/O_2 can trap some of the electron charge from the NTO/STO CB (Figs. 4, S3, and S4 [9]). At low concentrations, O/O_2 bind with an energy gain as large as 3.5 eV per species. Adsorption of O_2 is thermodynamically favorable up to 100% surface coverage, whereas adsorption of O is favorable only up to 50% coverage in the case of NTO × 1 and up to 100% in NTO × 2 [Fig. 4(a)]. The amount of charge transferred to the adsorbed O (O_{ad}) scales linearly with O_{ad} coverage up to 50% in NTO × 1 and up to ∼90% in NTO × 2 [Fig. 4(b)], i.e., O_{ad} scavenges CB electrons from the surface and subsurface (in NTO × 2) TiO_2 planes, effectively depleting the lower Hubbard band of NTO. We found that applying the Hubbard U correction has a negligible effect of both the adsorption energies and the amount of transferred charge (Fig. S3 [9]). Adsorbed O_2 was found to behave in the same way, except that these species trap smaller amounts of the electron charge per adsorbate (Fig. S4 [9]). While the Bader population analysis suggests that only a fraction of the lower Hubbard band in NTO × 1 is depleted by the adsorbed O/O_2, analysis of the calculated electron density of states (DOS) for (Fig. S5 [9]) reveals that increasing O/O_2 coverage to 50% for O and to 100% for O_2 fully depletes the conduction band in the NTO × 1 case. Therefore we conclude that the formal oxidation states of these species are O^{2-} and O_2^-.

Assuming that SrO and TiO_2 planes are neutral and NdO planes carry a formal charge of $+1e$ per u.c., adsorption of O/O_2 creates a near-surface electric field [Figs. 4(c) and S4(c) [9]]. NTO/STO heterostructures with more than two NTO layers will retain some of the CB electrons even after O_{ad} electron scavengers are fully saturated and all surface binding sites are occupied. These CB electrons can screen the near-surface electric field. In contrast, in NTO × 1 and NTO × 2 such screening can occur only via redistribution of ions, for example, via incorporation of anions (e.g., formation of interstitial oxide species [37]), or emission of cations (e.g., formation of V_{Nd}). To quantify the energetics of V_{Nd} formation, we calculated the energy cost (ΔE) of displacing an Nd atom from the subsurface NdO plane into the adatom (Nd_{ad}) configuration, i.e., the formation of the V_{Nd}-Nd_{ad} defect pair. Examples of the resulting configurations, where the Nd_{ad} (in its Nd^{3+} charge state) is coordinated by either O^{2-} or O_2^-, are shown in Fig. 5. We find that the energy change (ΔE) associated with this process depends on the type of the surface oxygen species and on their local surface density. For example, the formation of V_{Nd}-Nd_{ad} defect where Nd_{ad} is coordinated with two O^{2-} ions [Fig. 5(a)] is thermodynamically unfavorable with the energy cost of ∼0.8 eV. However, it becomes strongly

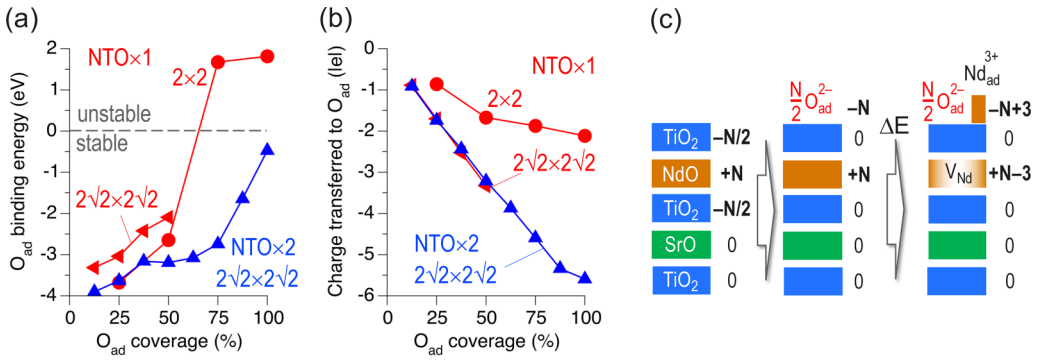

FIG. 4. Interaction of oxygen atoms with NTO/STO based on *ab initio* simulations. (a) Binding energies of O adatoms (O_{ad}) to the TiO_2 surface of NTO (1 u.c.)/STO (NTO × 1) and NTO (2 u.c.)/STO (NTO × 2) decrease with O_{ad} coverage; maximum O_{ad} coverage reaches 50% and 100% in NTO × 1 and NTO × 2, respectively. Binding energies correspond to the energy gain due to sequential addition of $1/2O_2$. (b) Total electron charge transferred from NTO/STO to O_{ad} increases with coverage, thus creating a negatively charged surface layer. (c) Schematics of the charge density redistribution in NTO × 1 (lateral cell containing N Nd atoms) induced by O_{ad}. The formal charges per each atomic plane of the supercell are given in the units of $|e|$; ΔE indicates the energy needed to displace an Nd^{3+} ion into the adatom (Nd_{ad}) configuration.

preferred if the number of the O^{2-} ions near Nd_{ad} increases to 4 ($\Delta E \sim -1.2$ eV), as shown in Fig. 5(b). Very similar values of ΔE were obtained using the PBEsol + U approach: +0.8 and –1.3 eV, respectively. We find that adsorbed O^{2-} ions have a qualitatively similar effect on the V_{Nd}-Nd_{ad} stability: the calculated ΔE is +0.7 and –0.8 eV for the case of two and four O_2^- ions near the Nd_{ad}, respectively [Figs. 5(c) and 5(d)]. Applying the +U correction leads to nearly identical ΔE values (+0.8 and –0.8 eV).

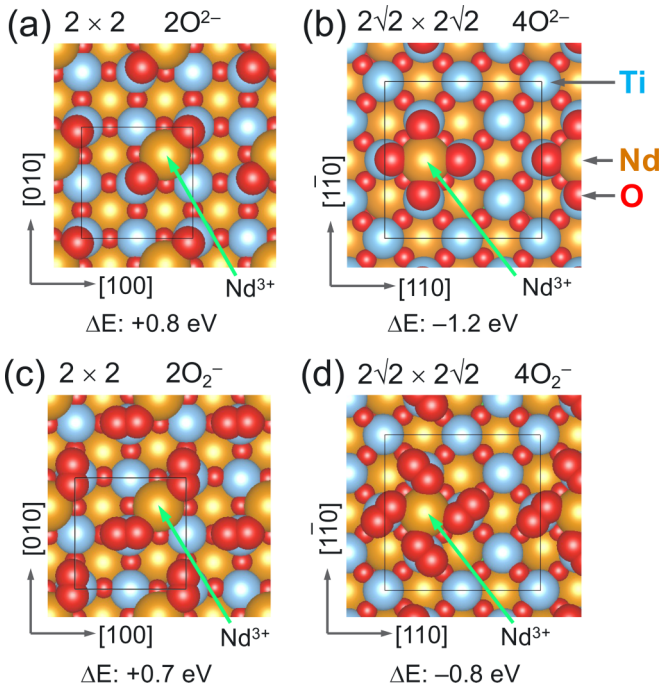

FIG. 5. Nd^{3+} in the adatom (Nd_{ad}) configuration coordinated with two and four O^{2-} (a), (b) and O_2^- (c), (d) ions on the TiO_2-terminated surface of NTO monolayer supported on STO. ΔE shows energy cost ($\Delta E > 0$) and gain ($\Delta E < 0$) due to transferring a single Nd^{3+} ion from the NdO plane to the Nd_{ad} site in the 2 × 2 (a), (c) and $2\sqrt{2} \times 2\sqrt{2}$ (b), (d) lateral cells. The displaced Nd atoms are indicated with green arrows; adsorbed O/O_2 species are shown with large red spheres.

The magnitude of ΔE plotted as a function of the number of adsorbed O^{2-} in the adatom configuration (O_{ad}^{2-}) [Fig. 6(a)] shows that the V_{Nd}-Nd_{ad} defect becomes stable if the fraction of the surface sites occupied with O_{ad}^{2-} ([O_{ad}]) is ~2.5/8 or higher. Interestingly, the slope of ΔE vs [O_{ad}] is identical for NTO × 1 and NTO × 2 up to 50% O_{ad}^{2-} coverage, i.e., until all surface Ti^{3+} are converted to Ti^{4+}. In the case of NTO × 2, this slope decreases for [O_{ad}] > 4/8, indicating that scavenging CB electrons from the subsurface TiO_2 plane in NTO × 2 is thermodynamically less favorable than that from the surface TiO_2 plane [Fig. 6(a)].

The calculated barrier for displacing a subsurface Nd into the Nd_{ad} configuration is ~3 eV [inset in Fig. 6(a)], while the barrier for Nd_{ad} in-diffusion can be over 3.5 eV if it is coordinated by three O_{ad}^{2-} and as high as 4.5 eV if it is coordinated by four O_{ad}^{2-}. We propose that these barriers can be avoided if a fraction of the incoming Nd atoms is stabilized

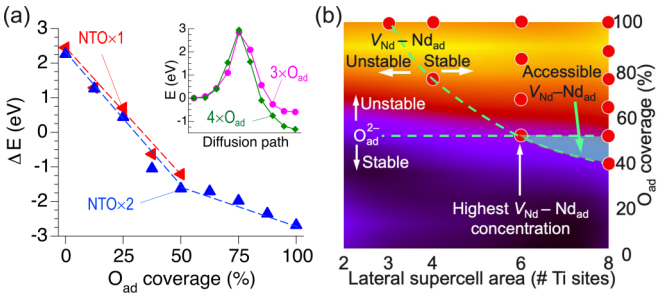

FIG. 6. (a) The dependence of ΔE on the O_{ad} coverage ($2\sqrt{2} \times 2\sqrt{2}$ lateral cell) shows that the formation of V_{Nd}-Nd_{ad} is thermodynamically preferred if Nd_{ad} is coordinated by three or more O_{ad}. Inset: potential energy profiles for Nd diffusion from the NdO plane (left) into the Nd_{ad} site (right) coordinated by three and four O_{ad}. (b) Overlap of the stability regions for the surface O_{ad} (darker colors indicate stronger O_{ad} binding) and V_{Nd}-Nd_{ad} defects (red circles) depending on the O_{ad} coverage and the size of the lateral cell in NTO × 1 shows the onset of the V_{Nd} formation.

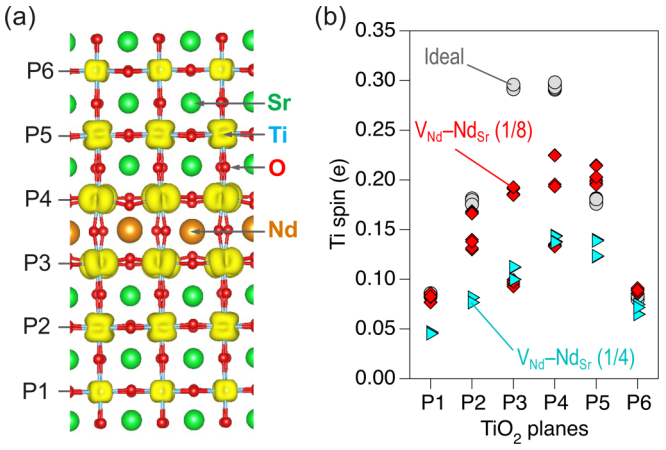

FIG. 7. (a) Structure of the STO/NTO (1 u.c.)/STO slab terminated with SrO planes and a surface of the constant spin density (yellow) calculated using PBEsol + U (Ti 3d); P1–P6 label TiO_2 planes across the slab. (b) Electron spin associated with each Ti ion in the ideal STO/NTO (1 u.c.)/STO heterostructure and in the presence of V_{Nd}-Nd_{Sr} defects at the lateral concentrations of 1/8 and 1/4. The V_{Nd}-Nd_{Sr} defects deplete the conduction band as manifested by the lower amount of the Ti electron spin. This effect is stronger for the Ti atoms located closer to V_{Nd} and for larger V_{Nd}-Nd_{Sr} concentrations.

by adsorbed O/O_2 in the Nd_{ad} configuration before they can occupy their lattice sites; accordingly, their lattice sites in the NdO plane remain unfilled, thus creating an accompanying V_{Nd}. To summarize, V_{Nd}-Nd_{ad} defects form if the surface binds O/O_2 at sufficiently high local concentrations to preferentially stabilize Nd in the adatom configuration over the ideal lattice configuration.

To determine the concentration of such V_{Nd}-Nd_{ad} defects in NTO × 1, we calculated the coverage-dependent energy gain due to binding O atoms in the O_{ad}^{2-} configuration for several lateral supercells containing between 2 and 8 surface Ti species. The resulting energy surface is shown as a heat map in Fig. 6(b): in all cases O_{ad}^{2-} are stable up to, but not in excess of, 50% coverage. Red circles in Fig. 6(b) show configurations where the formation of a V_{Nd}-Nd_{ad} defect is thermodynamically preferred. The overlap of the regions where O_{ad}^{2-} and V_{Nd}-Nd_{ad} are simultaneously stable define the conditions at which the formation of V_{Nd}-Nd_{ad} is possible. Accordingly, the onset of their formation is given by the vertex that corresponds to 50% O_{ad}^{2-} coverage for every six Ti surface sites. Thus, we estimate $[V_{Nd}] \approx 1/6$ per Nd atom in NTO × 1, which agrees well with the results of COBRA. A similar process and comparable energetics are expected for NTO × 2. However, in this case, V_{Nd} can spread out homogenously between the two NdO layers after the growth is completed, thus resulting in $[V_{Nd}]$ of $\sim 1/12$ per Nd atom. This value of $[V_{Nd}]$ is beyond the uncertainty limits of the integrated EN calculation in COBRA, making it challenging to detect.

To link the V_{Nd}-Nd_{ad} defects to the results of the transport measurements, we examine the charge distribution in the STO/NTO (1 u.c.)/STO heterostructure with and without this defect. The heterostructure was capped with SrO planes on both sides to eliminate surface effects (Fig. 7). In the ideal STO/NTO (1 u.c.)/STO, the CB electrons concentration is largest near the NdO plane, homogeneous in plane, and symmetric on both sides of the heterostructure [Fig. 7(b)]. However, in the presence of V_{Nd}-Nd_{Sr} defects, the CB is depleted in the vicinity of the V_{Nd}, which affects both the magnitude of the charge associated with Ti 3d orbitals and the spatial distribution of the spin density. In particular, since V_{Nd}-Nd_{Sr} defects break the lateral symmetry of the heterojunction, the symmetry of the electron distribution over the Ti 3d orbitals, as represented by the electron spin associated with Ti 3d, becomes broken as well. As shown in Fig. 7(b), the larger amount of spin is associated with STO/NTO interface than with NTO/STO interface. This is consistent with the observed asymmetric distribution of Ti^{3+} species reported earlier (see Fig. 4 in Ref. [10]) and suggests that the formation of the V_{Nd}-Nd_{Sr} defect pairs underpins the formation of diffuse NTO/STO interfaces. Finally, for $[V_{Nd}-Nd_{Sr}] = 1/6$, the remaining 2DEG charge density is 0.33 e^-/u.c./interface which compares well with the experimental value of $n_{2D} =$ 0.25 e^-/u.c./interface. We also must consider the possibility that Nd_{ad} are displaced by Sr at the time of STO deposition on NTO. In this case, the remaining defect (V_{Nd}) generates a n_{2D} value of exactly 0.25 e^-/u.c./interface.

This mechanism of V_{Nd} and V_{Nd}-Nd_{Sr} defect formation by the oxygen scavengers can be extended to larger NTO thicknesses. In this case, the accumulation of V_{Nd} and displaced Nd may result in the apparent Sr-Nd intermixing reported previously at the STO/NTO interfaces [10]. For thick NTO, $[V_{Nd}]$ approaches zero and n_{2D} approaches 1 e^-/u.c. of NTO, consistent with n_{2D} measurements. This mechanism stems from the ability of the oxygen species adsorbed at the surface to trap electron charge and, therefore, create near-surface electric field. This effect is independent of the synthesis approach if (i) O/O_2 or any other electron scavenger is present at the growth front and (ii) the material in question is ionic, i.e., the near-surface electric field is compensated for by rearrangements of the neighboring ionic species.

IV. SUMMARY

We reveal that excess oxygen accumulating during NTO growth promotes the formation of V_{Nd} in NTO × 1 and thus lowering of the 2DEG n_{2D}. We also show with first principles calculations that V_{Nd} formation in NTO layers is driven not by thermodynamic factors alone, but by kinetic processes at the STO/NTO growth front. We present a mechanism applicable to any NTO thickness that is consistent with both COBRA results and n_{2D} measurements. We explain why V_{Nd} are reliably detectable only in NTO × 1, where $[V_{Nd}]$ reaches a value of $\sim$1/6 per Nd atom. The general theme of n_{2D} control by means of defect engineering constitutes a fruitful line of future investigation. Utilizing electron scavengers that are more aggressive than oxygen, or displacing electron scavengers with inert gases, could be used to control $[V_{Nd}]$ as well as vacancies of other A-site species and therefore the 2D carrier density.

ACKNOWLEDGMENTS

Work at PNNL was supported by U.S. Department of Energy (DOE), Office of Science (SC), Basic Energy Sciences

under Award No. 10122. PNNL is a multiprogram national laboratory operated for the DOE by Battelle Memorial Institute under Contract No. DE-AC05-76RL0-1830. W.S.S. acknowledges the support from OSU-PNNL Graduate Fellowship. Work at UMN was supported by the U.S. DOE through DE-SC0020211. The surface XRD was carried out at beamline 33-ID of the Advanced Photon Source, a DOE SC User Facility, operated for the DOE SC by Argonne National Laboratory under Contract No. DE-AC02-06CH11357. This research used resources of the National Energy Research Scientific Computing Center (NERSC), a DOE SC User Facility supported by the SC of the U.S. DOE under Contract No. DE-AC02-05CH11231 using NERSC Award No. BES-ERCAP0021800.

[1] J. Heber, Nature (London) **459**, 28 (2009).
[2] J. Mannhart and D. G. Schlom, Science **327**, 1607 (2010).
[3] P. Xu, Y. Ayino, C. Cheng, V. S. Pribiag, R. B. Comes, P. V. Sushko, S. A. Chambers, and B. Jalan, Phys. Rev. Lett. **117**, 106803 (2016).
[4] A. Gozar, G. Logvenov, L. F. Kourkoutis, A. T. Bollinger, L. A. Giannuzzi, D. A. Muller, and I. Bozovic, Nature (London) **455**, 782 (2008).
[5] H. Y. Hwang, Y. Iwasa, M. Kawasaki, B. Keimer, N. Nagaosa, and Y. Tokura, Nat. Mater. **11**, 103 (2012).
[6] N. Nakagawa, H. Y. Hwang, and D. A. Muller, Nat. Mater. **5**, 204 (2006).
[7] M. Dyakonov and M. Shur, Phys. Rev. Lett. **71**, 2465 (1993).
[8] A. Ohtomo and H. Y. Hwang, Nature (London) **427**, 423 (2004).
[9] See Supplemental Material at http://link.aps.org/supplemental/10.1103/PhysRevMaterials.6.103405 for experimental methods.
[10] P. Xu, T. C. Droubay, J. S. Jeong, K. A. Mkhoyan, P. V. Sushko, S. A. Chambers, and B. Jalan, Adv. Mater. Interfaces **3**, 1500432 (2016).
[11] Y. Oh, H. Kim, K. Baek, L. Do, G. Lee, and C. Kang, Sci. Adv. Mater. **10**, 518 (2018).
[12] K. H. L. Zhang, P. V. Sushko, R. Colby, Y. Du, M. E. Bowden, and S. A. Chambers, Nat. Commun. **5**, 4669 (2014).
[13] S. R. Spurgeon, Y. Du, T. Droubay, A. Devraj, X. Sang, P. Longo, P. Yan, P. G. Kotula, V. Shuttanandan, M. E. Bowden, J. M. LeBeau, C. Wang, P. V. Sushko, and S. A. Chambers, Chem. Mater. **28**, 3814 (2016).
[14] T. Berger, M. Sterrer, O. Diwald, and E. Knözinger, Chem. Phys. Chem. **6**, 2104 (2005).
[15] X. Zhao, J. Chen, and N.-G. Park, Sol. RPL **3**, 1800339 (2019).
[16] K. O. Kirlikovali, Z. Chen, X. Wang, M. R. Mian, S. Alayoglu, T. Islamoglu, and O. K. Farha, ACS Appl. Mater. Interfaces **14**, 3048 (2022).
[17] S. E. Nunes, L. C. Matte, and C. R. Cunha, Mater. Res. Express **9**, 095905 (2019).
[18] Y. Yacoby, H. Zhou, R. Pindak, and I. Božović, Phys. Rev. B **87**, 014108 (2013).
[19] Y. Yacoby, M. Sowwan, E. Stern, J. O. Cross, D. Brewe, R. Pindak, J. Pitney, E. M. Dufresne, and R. Clarke, Nat. Mater. **1**, 99 (2002).
[20] Y. Yacoby, C. Brooks, D. Schlom, J. O. Cross, D. A. Walko, C. N. Cionca, N. S. Husseini, A. Riposan, and R. Clarke, Phys. Rev. B **77**, 195426 (2008).
[21] Z. Feng, Y. Yacoby, W. T. Hong, H. Zhou, M. D. Biegalski, H. M. Christen, and Y. Shao-Horn, Energy Environ. Sci. **7**, 1166 (2014).
[22] Z. Feng, W. T. Hong, D. D. Fong, Y.-L. Lee, Y. Yacoby, D. Morgan, and Y. Shao-Horn, Acc. Chem. Res. **49**, 966 (2016).
[23] J. S. Jeong, M. Topsakal, P. Xu, B. Jalan, R. M. Wentzcovitch, and K. A. Mkhoyan, Nano Lett. **16**, 6816 (2016).
[24] M. Sowwan, Y. Yacoby, J. Pitney, R. MacHarrie, M. Hong, J. Cross, D. A. Walko, R. Clarke, R. Pindak, and E. A. Stern, Phys. Rev. B **66**, 205311 (2002).
[25] G. Kresse and J. Furthmüller, Phys. Rev. B **54**, 11169 (1996).
[26] J. P. Perdew, A. Ruzsinszky, G. I. Csonka, O. A. Vydrov, G. E. Scuseria, L. A. Constantin, X. Zhou, and K. Burke, Phys. Rev. Lett. **100**, 136406 (2008).
[27] S. L. Dudarev, G. A. Botton, S. Y. Savrasov, C. J. Humphreys, and A. P. Sutton, Phys. Rev. B **57**, 1505 (1998).
[28] P. E. Blöchl, Phys. Rev. B **50**, 17953 (1994).
[29] W. Tang, E. Sanville, and G. Henkelman, J. Phys.: Condens. Matter **21**, 084204 (2009).
[30] G. Henkelman, B. P. Uberuaga, and H. Jónsson, J. Chem. Phys. **113**, 9901 (2000).
[31] Z. Feng, Y. Yacoby, M. J. Gadre, Y. Lee, W. T. Hong, H. Zhou, M. D. Biegalski, H. M. Christen, S. B. Adler, D. Morgan, and Y. Shao-Horn, J. Phys. Chem. Lett. **5**, 1027 (2014).
[32] T. T. Fister, H. Zhou, Z. Luo, S. S. A. Seo, S. O. Hruszkewycz, D. L. Proffit, J. A. Eastman, P. H. Fuoss, P. M. Baldo, H. N. Lee, and D. D. Fong, APL Mater. **2**, 021102 (2014).
[33] H. Lee, N. Campbell, J. Lee, T. J. Asel, T. R. Paudel, H. Zhou, J. W. Lee, B. Noesges, J. Seo, B. Park, L. J. Brillson, S. H. Oh, E. Y. Tsymbal, M. S. Rzchowski, and C. B. Eom, Nat. Mater. **17**, 231 (2018).
[34] Y. Li, F. Wrobel, X. Yan, A. Bhattacharya, J. Sun, H. Hong, H. Zhou, H. Wang, and D. D. Fong, Appl. Phys. Lett. **118**, 061601 (2021).
[35] D. D. Fong, C. Cionca, Y. Yacoby, G. B. Stephenson, J. A. Eastman, P. H. Fuoss, S. K. Streiffer, C. Thompson, R. Clarke, R. Pindak, and E. A. Stern, Phys. Rev. B **71**, 144112 (2005).
[36] D. Ricci, C. Di Valentin, G. Pacchioni, P. V. Sushko, A. L. Shluger, and E. Giamello, J. Am. Chem. Soc. **125**, 738 (2003).
[37] R. B. Comes, P. Xu, B. Jalan, and S. A. Chambers, Appl. Phys. Lett. **107**, 131601 (2015).